Dynamical analysis of attosecond molecular modes

Wan-Dong Yu [1,*] Hao Liang,[1] Lei Geng [1] and Liang-You Peng[1,2,3,4,†]

[1]*State Key Laboratory for Mesoscopic Physics and Frontiers Science Center for Nano-optoelectronics,*
School of Physics, Peking University, 100871 Beijing, China
[2]*Collaborative Innovation Center of Quantum Matter, 100871 Beijing, China*
[3]*Collaborative Innovation Center of Extreme Optics, Shanxi University, 030006 Taiyuan, China*
[4]*Peking University Yangtze Delta Institute of Optoelectronics, 226010 Nantong, Jiangsu, China*

Attosecond charge migration (CM) modes in halogenated hydrocarbon chains are investigated from first principles. The initial hole state on the Br site is created by the constrained density functional theory (CDFT) and the following CM dynamics is tracked by the time-dependent density functional theory (TDDFT). We find the attosecond mode is mainly recorded in the spin channel where the electron is initially ionized. By employing approximate functionals at different theory levels, we find the local density approximation gives satisfactory results to reproduce the attosecond mode and more advanced exchange-correlation functionals do not affect the mode significantly. By alleviating the self-interaction error with an average density correction or allowing nuclei to relax, it is shown that the nuclear motion is a key factor to alter the mode. In addition, by a detailed analysis of single-electron orbitals, we find the attosecond mode is attributed to the electronic collective motion in the outermost energy shell. Our results will be useful in understanding the mechanism of molecular modes and motivating the ultrafast CM detection methods for future experiments.

I. INTRODUCTION

In the last few decades, the tremendous development of ultrashort light sources and laser pump-probe techniques made possible direct access to the electronic dynamics in molecules with subfemtosecond resolutions [1–3]. The observation of the electronic dynamics approaching the attosecond timescale is the first step to realizing the control and optimization of chemical and biophysical reactivities, which is essential to the attosecond molecular science [4–6]. In particular, the electronic dynamics driven by pure electron correlations, termed *charge migration*, is attracting great interest [7–9]. To the best of our knowledge, Cederbaum and Zobeley first predicted the existence of charge migration (CM) in polyatomic systems [10]. Nevertheless, the experimental demonstration of attosecond CM was not achieved until 2014 [11]. CM involves a rapid redistribution of charge density before the nuclear dynamics takes place and usually survives less than 10 femtoseconds (fs) from the initial ionization or excitation [12–14]. Using full-dimensional quantum calculations, Despré *et al.* predicted long-time charge migration (more than 10 fs) in ionized acid molecules before getting trapped by the nuclear motion [15]. Therefore, CM offers a direct way to understand the complex many-body correlations in the early stage of a nonstationary system, which has been shown to impact the subsequent electron-nuclear dynamics, such as bond rearrangement [16], dissociation [17], and relaxation [18].

Characterizing CM requires access to both the spatial and temporal information of charge distributions, including the intramolecular charge localization, the migration distance, the oscillation frequency, and so on. In experiments, this can be achieved using the reconstruction of charge density by pump-probe ionization. For instance, Calegari *et al.* identified a sub-4.5-fs charge oscillation in phenylalanines, suggesting highly correlated dynamics between the hole density and the incident laser pulse [11]. Using the high-harmonic spectroscopy (HHS) by strong laser pulses, Karus *et al.* reconstructed the attosecond CM in ionized iodoacetylene [8]. Recently, He *et al.* filmed movies of the attosecond CM in small single molecules at time steps of 50 attoseconds, pointing out a swirling motion of the holes [19]. Using x-ray attosecond transient-absorption spectroscopy, Matselyukh *et al.* reported an interesting revival of the charge migration in the neutral silane [20]. In theory, a large number of *ab initio* calculations were carried out [10,12,13,21–30], as the CM mechanism was not possible to be understood on the grounds of the available experiments alone. These calculations showed that both many-electron correlations and nuclear dephasing play a key role in CM.

Recently, an interesting feature of CM in halogenated hydrocarbon chains was predicted by Folorunso *et al.* in their pioneering work [31–33]. They found that the site-specific hole density can migrate across the entire carbon skeleton of halogenated hydrocarbon chains via *attosecond molecular modes*. Different from the previous studies in which the electronic density swings between two close functional groups [34] or fluctuates around one molecular site [35], such harmonic hole modes have a low characteristic frequency

---

*wandongyu@pku.edu.cn
†liangyou.peng@pku.edu.cn

($\sim$1 eV), and more importantly, are related to a long-distance (up to $\sim$17 Å) hole migration from the halogen site to the terminal carbon-carbon bond. From the viewpoint of quantum oscillations, the complicated many-body effect may be encoded in both the spatial charge distributions and the harmonic modes. Some mechanisms and features of CM were discussed, such as the bond hopping mechanism [36], the functional-group dependence [31], the two-state oscillation mechanism [34], and the nuclear decoherence effect [26]. However, the attosecond mode in halogenated hydrocarbon chains has not been fully understood.

In this paper, we focus on the attosecond modes in halogenated hydrocarbon chains. Our motivations spring from trying to study the electron-correlation properties of the modes, such as the roles of the initial state and the electronic exchange-correlation, and then trying to understand the quantum nature of the modes. In the present work, we choose bromoacetylene (BrC_2H) as an example, mainly due to the following three reasons. (i) Experiments showed that a site-specific hole can be created in halogenated acetylene by the strong-field ionization (SFI) [8] and the hole around the halogen site provides a highly sensitive interaction with the probe pulse [11]. (ii) BrC_2H, as well as more complicated halogenated hydrocarbon chains, are polar molecules, and multiple excited states of the cation can be populated by SFI. In experiments, polar molecules can be aligned or oriented using the impulsive orientation technique [37], such as the iodoacetylene alignment control in Ref. [8]. Effective control of the molecular orientation may improve the precision of CM measurements. (iii) BrC_2H encompasses several common structural characteristics of halogenated hydrocarbon chains. For example, BrC_2H has a short carbon-carbon (C-C) bond, axial symmetry, and conjugated molecular orbitals, serving as a good candidate among the family of halogenated hydrocarbon chains.

Analogous to Refs. [31,32], we employ the constrained density functional theory (CDFT) for initializing the SFI hole density. CDFT has been proven to be a valuable method for electronic structure calculations [38]. At a basic level, CDFT provides opportunities to work around some detrimental problems in (TD)DFT, such as the long-range electronic transfer [39], the excited states approaching conical intersections [40], and the self-interaction error (SIE) [41]. In the present work, the CDFT hole state is related to multiple Kohn-Sham orbitals (KSOs). The corresponding CDFT hole density is not initialized in a single KSO, but distributed among multiple KSOs. The initial hole state created by CDFT has been shown to give more reasonable charge dynamics, as well as a stronger current density than the sudden removal of electrons from occupied KSOs [42]. Starting with the CDFT initial state, the following CM dynamics is tracked using the time-dependent density functional theory (TDDFT) [43], which has a good record for correctly capturing some challenging electronic processes in molecules, such as the high harmonic generation [44], the charge transfer [45], the double excitation [46], and the strong-field dynamics [47].

In principle, TDDFT is a formally exact method for many-electron systems. However, dynamical simulations with TDDFT usually confront two sources of error. On the one side, the exact form of the exchange-correlation functional is unknown, so in most situations only approximate functionals are used to simulate the dynamics. Generally, there are two levels of approximations, i.e., exchange-correlation functionals from static DFT ignore memory effects and the static functional itself is an approximately closed form. Therefore, in the present work, it is necessary to verify the effects of approximate DFT functionals, for instance, SIE [48,49] or incorrect (spatial) asymptotic behaviors [50]. In addition, the CM dynamics can be highly sensitive to the choice of the initial state [28,42,51]. In this paper, we will discuss how these issues impact the attosecond mode to some extent.

The rest of the paper is organized as follows. In Sec. II, we briefly recall the framework of CDFT. In Sec. III, we present the computed CM for $[BrC_2H]^+$ and discuss the spin-dependent CM dynamics. In Sec. IV, a brief conclusion is presented. Finally, the Appendixes are given for the dynamical properties of the $[BrC_4H]^+$.

II. METHODS

A. Constrained density functional theory

The site-specific hole density created by SFI is modeled using the CDFT. In a standard CDFT framework, one or more constraints can be applied to the electronic density (see more details in Refs. [39,42] and the review article [38]). One can suppose there are total m constraints in an N-electron system. In general, the kth constraint for the σ-spin channel can be written as

$$\int w_k^\sigma(\mathbf{r})\rho_\sigma(\mathbf{r}) - F_k^\sigma = 0, \qquad (1)$$

where σ denotes the electronic spin, which has two opposite components, i.e., $\uparrow$ and $\downarrow$. $w_k^\sigma(\mathbf{r})$ is the weight function that defines the way of applying the kth constraint on the σ-spin density. F_k^σ is the value of the kth constraint.

In the Kohn-Sham (KS) formalism [52], the total energy of the N-electron system is a functional of the electronic density

$$E[\rho] = T + \int d\mathbf{r}\, v_n(\mathbf{r})\rho(\mathbf{r}) + J[\rho] + E_{xc}[\rho_\uparrow, \rho_\downarrow], \qquad (2)$$

where T is the single-electron kinetic energy (in atomic units)

$$T = \sum_{\sigma=\uparrow,\downarrow} \sum_{i=1}^{N_\sigma} \left\langle \psi_{i,\sigma} \left| -\frac{\nabla^2}{2} \right| \psi_{i,\sigma} \right\rangle, \qquad (3)$$

v_n is the external potential, J is the classical Coulomb energy, E_{xc} is the exchange-correlation energy, and $\psi_{i,\sigma}$ is the ith σ-spin KSO. N_σ is the number of σ-spin electrons ($N_\uparrow + N_\downarrow = N$). The total density ρ is calculated by summing up all the spin-up and -down densities

$$\rho = \sum_{\sigma=\uparrow,\downarrow} \sum_{i=1}^{N_\sigma} f_{i,\sigma} |\psi_{i,\sigma}(\mathbf{r})|^2, \qquad (4)$$

where $f_{i,\sigma}$ are occupation numbers.

The goal of CDFT is to minimize the DFT energy functional ($E[\rho]$) under all the constraints in Eq. (1). To this end, we can create a set of Lagrange multipliers ($\{\lambda_k\}$) to build the

following Lagrange energy functional:

$$\mathcal{L}[\rho, \{\lambda_k\}] = E[\rho] + \sum_{k=1}^{m} \lambda_k \left(\int w_k^\sigma(\mathbf{r})\rho_\sigma(\mathbf{r}) - F_k^\sigma \right). \quad (5)$$

The stationary conditions of $\mathcal{L}$ for normalized orbitals give the following equations:

$$\left[H_{\text{KS}} + \sum_{k=1}^{m} \lambda_k w_k^\sigma(\mathbf{r}) \right] \psi_{i,\sigma}(\mathbf{r}) = \varepsilon_i \psi_{i,\sigma}(\mathbf{r}), \quad (6)$$

where H_{KS} is the standard KS Hamiltonian

$$H_{\text{KS}} = -\frac{\nabla^2}{2} + v_n + \int \frac{\rho(\mathbf{r}')}{|\mathbf{r} - \mathbf{r}'|} d\mathbf{r}' + v_{\text{xc}}^\sigma(\mathbf{r}). \quad (7)$$

Thus, Eq. (6) is the standard KS equation except for the addition of constraint potentials, $\lambda_k w_k^\sigma(\mathbf{r})$. Solving Eq. (6) self-consistently together with Eq. (1) to yield λ_k and ψ_i ensures the constraints to be satisfied. To obtain λ_k, Wu et al. proposed a fast updating scheme that transfers the complicated eigenvalue problem into an optimizing search process [53]. Further discussions about the CDFT computational optimization can be found in Refs. [54,55] and the references therein.

To mimic the site-specific hole density created by SFI, the constraint is defined as the charge density difference between the donor (D) and the acceptor (A) group, i.e., $F_k^\sigma = N_\sigma^D - N_\sigma^A$. By following the w_k^σ definition by Wu et al. [53], in the coordinate space belonging to the D group, the sign of w_k^σ is defined to be positive, whereas in the coordinate space belonging to the A group, the sign of w_k^σ is defined to be negative. In this way, the constraint value F_k^σ designs the charge partition between the D and the A groups. For example, $F_k^\sigma = 0$ means the charge is equally divided and $F_k^\sigma < 0$ means more charge is assigned to the A group. By regulating the F_k^σ value, a desired charge imbalance between the two groups can be achieved.

Several options are available for the choice of the weight function w_k^σ [53], such as the Mulliken population [56], the modified Löwdin population [57], real-space partitions as suggested by Becke [58], and the Hirshfeld method [59]. In this work, we employ the Hirshfeld partition method and thus the weight function w_k^σ can be defined as [55]

$$w_k^\sigma(\mathbf{r}) = \frac{\sum_{I \in D} \rho_\sigma^I(\mathbf{r} - \mathbf{R}_I) - \sum_{I \in A} \rho_\sigma^I(\mathbf{r} - \mathbf{R}_I)}{\sum_I \rho_\sigma^I(\mathbf{r} - \mathbf{R}_I)}, \quad (8)$$

where $\rho_\sigma^I(\mathbf{r} - \mathbf{R}_I)$ denotes the free-atom ground-state electronic density of the Ith atom at the distance $\mathbf{r}$ from the atomic position $\mathbf{R}_I$. Since the Hirshfeld partition method is a real space formalism, we are able to perform CDFT calculations in the real-space DFT.

Note that, CDFT is only used to create the initial state. The constraints are dropped at the beginning of the time-dependent (TD) propagation ($t = 0$) so that the CDFT initial state is not the stationary state of the H_{KS} and the system will evolve in time.

B. Numerical details

All the calculations are carried out in a developmental version of the OCTOPUS program [60]. We implement CDFT
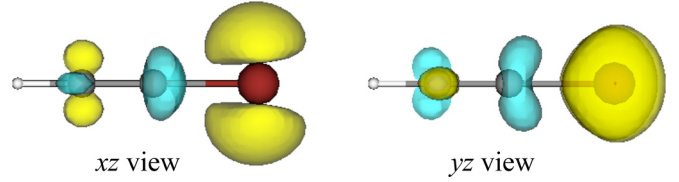

FIG. 1. Converged three-dimensional hole density $\rho^H(\mathbf{r}, t)$ of the $[BrC_2H]^+$ computed by CDFT under the constraint that a unit hole localizes on the Br site. Golden isosurfaces: positive parts of the hole density with the fixed value of $0.01\ a_0^{-3}$. Cyan isosurfaces: negative parts of the hole density with the fixed value of $-0.01\ a_0^{-3}$. Small balls: hydrogen atom. Middle-sized balls: carbon atom. Big balls: bromine atom.

calculations in OCTOPUS. To solve Eq. (6) under constraints, we adopt the fast updating scheme proposed by Wu et al. in Ref. [53], in which the constraint functions in Eq. (1) can be satisfied using a root-finding algorithm implemented on the basis of a standard DFT self-consistent loop. All numerical quantities are discretized in a cubic box ($52 \times 52 \times 52\ a_0^3$) with a uniform grid spacing of $0.27\ a_0$. The halogenated hydrocarbon chains are always aligned in the Z axis. The atomic core electrons are handled with norm-conserving pseudopotentials [61]. The Hirshfeld partition [59] method is used to calculate the weight function $w_k^\sigma(\mathbf{r})$. In all the calculations, the nuclei are fixed at the equilibrium positions of the neutral molecule. In CDFT calculations, we first set the occupation number of a highest-occupied molecular orbital (HOMO) electron of the neutral molecule to zero, and then, by fixing the occupation numbers, we perform CDFT self-consistency directly on the cation. In TD simulations, the iteration time step is fixed to 6.04×10^{-4} fs. In this work, we only consider the cationic case that an electron is initially ionized from the HOMO and the three-dimensional hole density $\rho^H(\mathbf{r}, t)$ is defined as the difference between the neutral ground-state electronic density $\rho^0(\mathbf{r})$ and the cationic density $\rho^+(\mathbf{r}, t)$,

$$\rho^H(\mathbf{r}, t) = \rho^0(\mathbf{r}) - \rho^+(\mathbf{r}, t). \quad (9)$$

Since hole distributions of the molecular ion are symmetric with respect to the molecular axis (i.e., the z axis), for the convenience of analysis, we define the following one-dimensional integrated hole density:

$$\rho^h(z, t) = \int \rho^H(x, y, z, t) dx dy. \quad (10)$$

As an example, Fig. 1 shows the $[BrC_2H]^+$ hole density created by SFI using CDFT with an adiabatic local density approximation (LDA) [62]. Here, the $[BrC_2H]^+$ cation has 15 valence electrons and the occupation number of a HOMO electron in the spin-up channel is set to 0. To constrain a unit hole around the Br atom, we impose a charge difference between the D group (Br) and the A group (C_2H). The resulting constraint value $F_k = -3.2030$, and the corresponding Lagrange multiplier $\lambda_k = -0.2138$ Hartree.

III. RESULTS AND DISCUSSIONS

In the following calculations, for all the molecular cations, a spin-up electron is ionized from the HOMO by setting its
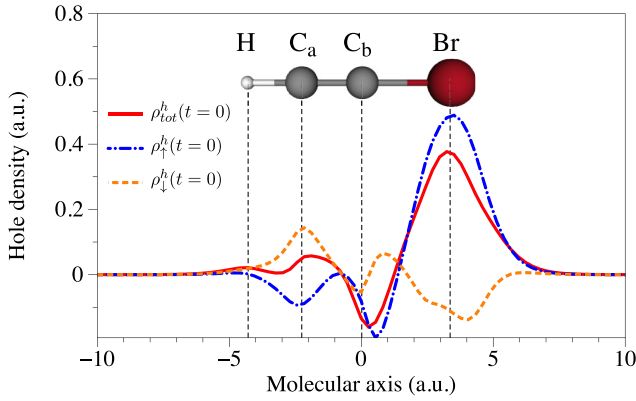
FIG. 2. One-dimensional integrated hole density along the $[BrC_2H]^+$ molecular axis created by CDFT with LDA. The total hole density (ρ_{tot}^h, solid curves) consists of two components, i.e., the spin-up hole density ($\rho_\uparrow^h$, dot-dashed curves) and the spin-down hole density ($\rho_\downarrow^h$, dashed curves). Vertical dashed lines are drawn to guide eyes.

occupation number to 0, and the initial hole state is always the CDFT state that constrains a unit hole on the Br site. The one-dimensional total hole density (ρ_{tot}^h) consists of two components, i.e., the spin-up ($\rho_\uparrow^h$) and -down ($\rho_\downarrow^h$) density. At any time, the total hole density is normalized to 1 since the $[BrC_2H]^+$ takes a unit of positive charge.

A. Spin-separated hole migration

Figure 2 shows the initial hole density of the $[BrC_2H]^+$ created by CDFT with LDA. Overall, most of the positive parts of the total hole density (ρ_{tot}^h) concentrate on the Br site. For the two spin components, the hole distributions show significant differences. For the spin-up channel, positive parts of the hole density are almost entirely located on the Br site. On the contrary, for the spin-down channel, the positive hole density distributes on the carbon bond and the negative parts of the hole density is located on the Br site. Due to the initial removal of a spin-up electron, most of the positive holes are constrained on the spin-up channel. At $t = 0$, the maximum value of the $\rho_\uparrow^h$ density is roughly five times larger than that of the $\rho_\downarrow^h$ density.

For the initial LDA hole density in Fig. 2, the resulting hole migration is shown in Fig. 3. On the whole, the hole density seldom moves to the hydrogen site, and the to-and-fro hole migration ranges between the Br and the C-C bond. For the $\rho_{tot}^h(t)$ as shown in Fig. 3(a), it oscillates periodically with a period of ~1.46 fs. Interestingly, it is found that the mode is mainly recorded in the spin-up channel, while the spin-down component does not contribute significantly. These results show the following. (i) In the considered computational time, the mode is not damped or smeared by electronic correlations, although spin-up electrons couple with spin-down electrons through the KS mean field. Such a long-time sustaining CM mode differs from previous calculations in hexatriene molecules [36] in which hole migrations become spread over the entire system within ~5 fs. (ii) The CM mode is mainly recorded in the spin channel where the electron is initially ionized. In addition, it is emphasized that the
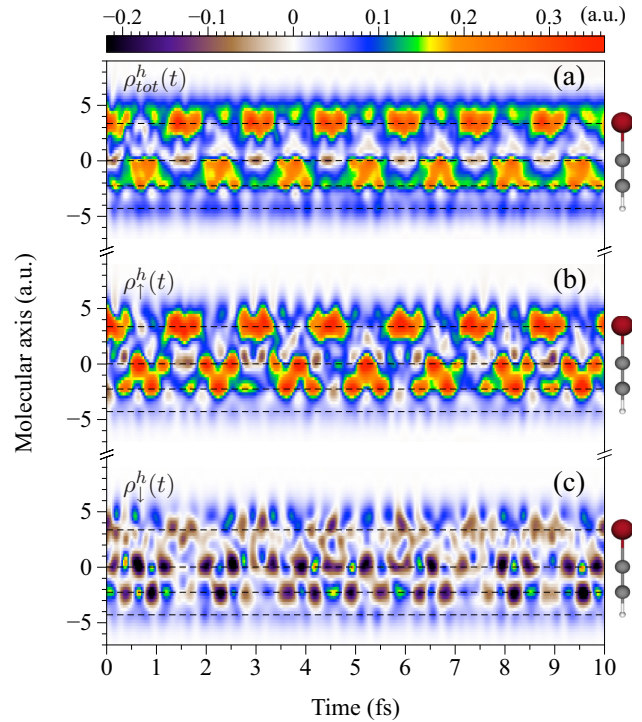

FIG. 3. Time evolution of the one-dimensional integrated hole density along the molecular axis by TDDFT with LDA. (a) Total hole density evolution $\rho_{tot}^h(t)$, and its two spin components, i.e., (b) the spin-up hole density $\rho_\uparrow^h(t)$ and (c) the spin-down hole density $\rho_\downarrow^h(t)$. Dashed lines are drawn to guide the eyes.

spin-separated CM behavior is also identified in more complex halogenated hydrocarbon chains and verified with more advanced exchange-correlation functionals. Moreover, it is not a surprise that the CM results of the two spin channels are different. The reason is that the dynamics start with spin-dependent cationic states in which a spin-up electron has already been ionized by setting its occupation number to zero. When such a spin-dependent initial state is propagated by the TDDFT under the present spin-symmetric Hamiltonian, we can expect that the two spin channels will show different dynamics.

B. Effects of electronic exchange-correlation and nuclear motion

In practical TDDFT simulations, the exact exchange-correlation functional is unknown, and thus only approximate functionals can be employed. The LDA and plenty of generalized gradient approximation (GGA) functionals were successfully applied in the calculations of electronic structures. However, for many purposes, these approximate functionals are not sufficiently accurate. Thus, in this section, we focus on some widely applied exchange-correlation functionals and we intend to clarify which effect is crucial to the mode.

Table I shows CM properties of the $[BrC_2H]^+$ cation. For each exchange-correlation functional the bond lengths are optimized in the neutral bromoacetylene. To characterize the CM mode in detail, we define three physical quantities, i.e., the CM distance, the CM time, and the corresponding CM speed.

TABLE I. CM properties of the $[BrC_2H]^+$ initiated with a unit hole localized on the Br site. For comparison, we list NIST bond lengths for the neutral BrC_2H geometry: $B_{C_bBr} = 3.39\ a_0$, $B_{C_aC_b} = 2.28\ a_0$, and $B_{HC_a} = 1.99\ a_0$ (a_0 is the Bohr radius).

	Bond length			CM properties		
F_{xc}	C_bBr (a_0)	C_aC_b (a_0)	C_aH (a_0)	Distance (a_0)	Time (fs)	Speed (a_0/fs)
LDA	3.35	2.27	2.03	4.48	0.73	6.14
LDA-EX	3.39	2.30	2.06	4.54	0.78	5.82
LDA + ADSIC	3.10	2.24	2.08	4.22	0.56	7.54
PBE	3.35	2.26	2.01	4.48	0.76	5.89
PBE0	3.35	2.25	2.00	4.47	0.74	6.04

Since the CM in halogenated hydrocarbon chains involves a harmonic oscillation from the halogen site to the terminal C-C bond, the CM distance is defined as the distance between the halogen and the middle point of the terminal C-C bond. The corresponding CM time is defined as the time to travel along the CM distance. In this work, CM time is obtained by fitting the total hole density $\rho_{tot}^h(t)$ with a cosine function and its precision is confirmed by the Fourier transform. The optimized LDA geometry is very close to the NIST data (see the caption of Table I for more details), within a relative error of ~2%.

In the LDA-EX functional, the LDA correlation part is dropped and thus only the LDA exchange energy remains. Compared to the LDA case, the LDA-EX neutral geometries do not vary a lot. The LDA-EX CM time is ~6% longer than the LDA case and the corresponding CM speed is ~5% faster. This suggests that the LDA correlation can alter the mode, but the mode change is not remarkable.

One of the major shortcomings of the LDA is that it is not free of the electronic self-interaction, leading to incorrect asymptotic behavior. Therefore, various procedures were developed to remove the SIE. Legrand *et al.* proposed a widely known SI correction, namely, average-density self-interaction-correction (ADSIC), for approximate exchange-correction energy functionals. The ADSIC modifies the KS mean-field potential on the basis of the average electronic density, rather than single electronic states. Here, we employ the ADSIC to alleviate the SIE of the LDA. In Table I, the neutral geometry given by the LDA + ADSIC shows that the bonds are close to the LDA case, except for the C_bBr bond, which is ~7% compressed. Compared with the LDA case, such bond compressing makes the LDA + ADSIC hole density move much faster, i.e., it takes ~23% shorter time to travel along the molecular bone.

The LDA + ADSIC results inspire us that the nuclear geometry may play an important role in altering the attosecond mode. Thus, by employing the Ehrenfest molecular dynamics [63] together with the TDDFT, we further study this problem by allowing the nuclei to relax. In the Ehrenfest-TDDFT formalism, the nuclei are described as classical point charges, nonadiabatically coupling with the electrons described by the TDDFT [64]. In simulations, the equation for the nuclear motion is solved by the velocity Verlet algorithm [65]. As shown in Fig. 4(a), we use the LDA initial conditions and
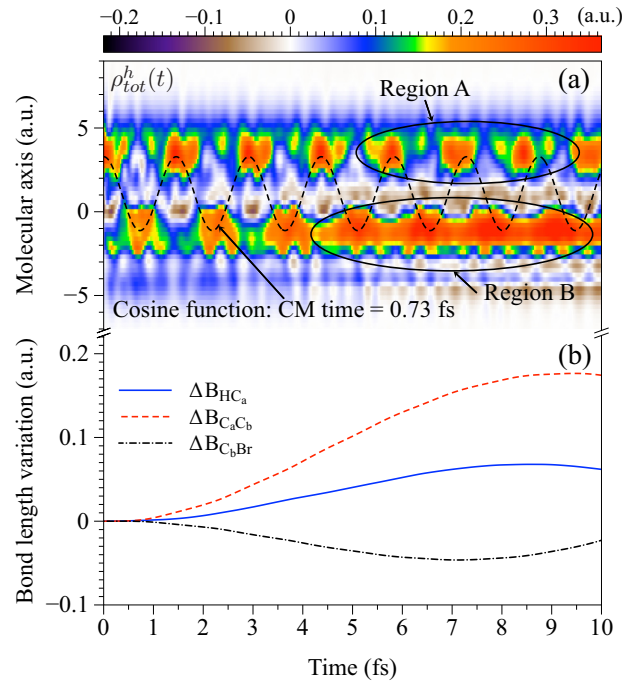

FIG. 4. (a) Rapid detuning and smearing of the LDA mode due to the nuclear relaxation. Dashed curves: a cosine function fitting the CM time of 0.73 fs. Regions A and B are drawn to guide the eyes. Region A: the detuning of the LDA mode. Region B: the smearing of the LDA mode. (b) Bond length variation, $\Delta B(t)$, defined as the bond length at time t minus the initial bond length, i.e., $\Delta B(t) = B(t) - B(t = 0)$.

the only difference is that, in the TD propagation, we allow the nuclear free relaxation along the molecular axis. In the early stage before ~4.5 fs, it is found that the hole density oscillates roughly for three periods, with a CM time of 0.73 fs. After 5 fs, as shown in region A, the mode is no longer the basic one with the CM time of 0.73 fs and it begins to detune to higher frequencies. It also suggests that, in the considered time, the initial CM mode cannot be retained for more than a few fs and then the nuclear motion can drive new modes with lower frequencies. In addition, as shown in region B, we find the hole density smears around the C-C bond, featuring the residual hole density that is difficult to get away from the C-C bond. Note that in Fig. 4 the nuclei are initially placed on the equilibrium positions of the neutral molecule, so the nuclear relaxation takes place due to the unbalanced forces acting on the nuclei. Compared to the bond lengths at $t = 0$, we evaluate that, at $t = 10$ fs, the bond length $B_{C_bC_b}$, B_{C_aH}, and B_{C_bBr} change roughly 8%, 3%, 1%, respectively. Therefore, for a polyatomic system at finite temperatures, the nuclear motion is not negligible and a certain mode of halogenated hydrocarbon chains may be hard to retain for more than a few fs.

The effect of the nuclear motion on the CM mode with other DFT functionals (e.g., LDA + ADSIC, PBE, and PBE0) is verified in the $[BrC_4H]^+$. For different functionals, our results (not shown) gives similar physical trends and the fast fading (i.e., smearing and detuning) of the CM mode is also identified after a few fs.

GGAs are a class of exchange-correlation functionals that depend on the electronic density and its spatial gradients. In this work, we employ a widely used GGA functional, the Perdew-Burke-Ernzerhof (PBE) [66], designed to satisfy energetically significant properties of the exact functional. As shown in Table I, the PBE neutral geometry is very close to that of the LDA. At the same time, the holes with PBE move slightly slower than that with LDA (within 5% difference), suggesting that the gradient approximate functional may not significantly change the attosecond mode. As a widely used hybrid functional, the PBE0 is designed by mixing a fraction of the exact exchange with GGA [67,68], which usually gives more satisfactory structural, kinetic, thermodynamic, and spectroscopic properties. Here, we employ a PBE0 functional mixing 25% of the exact exchange. Our results show that the PBE0 geometry is close to that of the LDA and the CM properties of the PBE0 do not show significant discrepancies. Notably, our PBE0 results differ from that in Ref. [31]. The CM distance in Ref. [31] is 4.73 a_0, larger than the present 4.47 a_0, and accordingly, the hole density in Ref. [31] spends more time of 0.92 fs to travel along the molecular bone. This discrepancy may originate from the following reasons: We employ the real-space Hirshfeld partition method to create the weight function and perform the real-space dynamics. These lead to different optimization structures as well as different initial CDFT states.

From the above results, we infer the following. (i) More advanced exchange-correlation functionals, such as the PBE and PBE0, do not significantly impact the attosecond mode. The mode can be depicted on the level of the LDA mean-field approximation. (ii) The change of the CM-involved bond length is an important factor in determining the attosecond mode. The LDA + ADSIC and the nuclear relaxation suggest that the nuclear motion affects the mode. This finding is consistent with previous studies, which showed that nuclear decoherence is a key factor to impact the CM dynamics in polyatomic molecules. Confirmed by both the semi-classical Ehrenfest [69,70] and fully quantum pictures [26], the zero-point energy of the ensemble of nuclear geometries leads to quick decoherence, roughly within 10 fs. Although the present $[BrC_2H]^+$ contains a light halogen atom, some results are comparable with more heavy $[IC_2H]^+$. For example, Kraus *et al.* experimentally reported the charge migration time of ~1.85 fs in $[IC_2H]^+$ [8], which is on the same order of magnitude as our results (~1.46 fs in $[BrC_2H]^+$ with LDA). Theoretically, Jia *et al.* studied the decoherence and recoherence of the charge migration in the $[IC_2H]^+$ [71]. They found that the first nuclear decoherence time is ~6 fs, which is close to our results in $[BrC_2H]^+$ with LDA (~5 fs). Also, Jia *et al.* found that nuclear decoherence may lead to trapped electrons, which is consistent with our finding that some holes smear around the C-C bond.

C. Charge collective motion in the outermost energy shell

Generally speaking, a full dynamical picture of the attosecond mode is described by the Schrödinger equation and the many-electron Hamiltonian is known. From the view of quantum mechanics, the CM mode is a linear interference problem because the CM many-electron state is the linear superposition of the eigenstates of the many-electron Hamiltonian. However, when the dynamics is handled with the KS-TDDFT, the CM mode turns to the problem that involves the nonlinear representation of occupied KSOs and all these occupied KSOs definitely do not form a complete set of the Hilbert space. In this section, we get insight into the nonlinear orbital behavior and find that the CM mode is a kind of electronic collective oscillation.

To quantify the intramolecular electronic motion, we employ the time-dependent average projection probability $P_\sigma(t)$, defined as the arithmetic mean of orbital projection probabilities

$$P_\sigma(t) = \frac{1}{D(\Omega)} \sum_{i \in \Omega} |\langle \psi_{i,\sigma}(t=0)|\psi_{i,\sigma}(t)\rangle|^2, \quad (11)$$

where Ω is a set of selected KSOs, and $D(\Omega)$ denotes the total number of elements in Ω. Since the CM mode is mainly recorded in the spin-up channel as discussed in Sec. III A, we therefore focus on the relevant spin-up probability $P_\uparrow(t)$ and from our analysis it is found that the $P_\downarrow(t)$ looks disordered and does not show any evident correspondence with the CM mode.

As shown in Fig. 5(b), we compute the average projection probability for the outermost four KSOs ($P_\uparrow^O$) and the rest of the inner KS orbitals ($P_\uparrow^I$). The outermost four orbitals refer to the initial highest four spin-up orbitals in the CDFT electronic state. At $t = 0$, the probability $P_\uparrow^O$ is 1, and then it oscillates in a broad region roughly from 0.21 to 0.92. Interestingly, it is found that the mode appears not only in the form of the hole density oscillation, but also in the form of electronic projection oscillation. To be specific, the $P_\uparrow^O$ oscillates in concert with the hole migration mode: The peaks of the $P_\uparrow^O$ correspond to the holes on the Br site and the valleys of $P_\uparrow^O$ correspond to the holes on the C-C site. On the contrary, such a concert evolution is not identified in the $P_\uparrow^I$. The attosecond mode is attributed to the electronic collective motion on the outermost four spin-up KSOs. In contrast, the electronic motion on the rest of the inner orbitals is disordered and does not show any uncluttered modes. Note that at $t = 0$, $P^O = 1$ is satisfied exactly because the CM dynamics starts with the CDFT initial hole state. However, in the subsequent TD propagation, the P^O cannot return to the value of $P^O = 1$, suggesting that the CM mode does not restore to the initial CDFT state.

To further understand the electronic motion, we plot the instantaneous energy expectation values for propagated KS orbitals as shown in Fig. 5(c). It is notable that the energy expectation values can be classified into two categories, i.e., the orbital energy shell formed by the outermost four KSOs ($E_\uparrow^O$), and that formed by the rest of the inner KSOs ($E_\uparrow^I$). The $E_\uparrow^O$ and $E_\uparrow^I$ are separated by a wide energy gap of ~4 eV, indicating the electronic motion on the outermost orbitals may not be strongly affected by that on the inner orbital shell. It is emphasized that a similar electronic collective motion is also verified in more complicated halogenated hydrocarbon chains, for example, the $[BrC_4H]^+$ as shown in Fig. 8 in Appendix A.

To get insight into the electronic collective motion of the $[BrC_2H]^+$ in the outermost energy shell, as shown in Fig. 10 in Appendix B, it is found that the spin-up CM mode is mainly attributed to the two π orbitals parallel to the xz plane, while
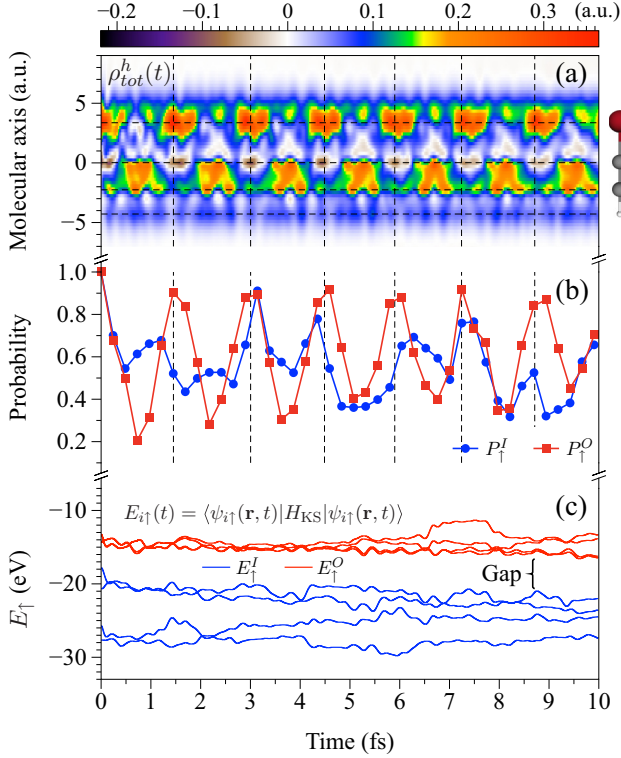
FIG. 5. Dynamical properties for the CM in the $[BrC_2H]^+$. (a) Time evolution of the one-dimensional total hole density, duplicated from Fig. 3(a) for comparison. (b) Time evolution of average projection probabilities for the spin-up channel. $P_\uparrow^O$: the outermost four KSOs. $P_\uparrow^I$: the rest of the inner KSOs. (c) Time evolution of instantaneous energy expectation values for the propagating spin-up KSOs. Red curves: the outermost four KSOs, forming the outermost orbital energy shell ($E_\uparrow^O$). Blue curves: the remaining four inner KSOs forming the inner orbital energy shell ($E_\uparrow^I$). Dashed lines are drawn to guide the eyes.

FIG. 6. Ensemble-TDDFT dynamical properties for the CM in the $[BrC_2H]^+$ using fractional occupation numbers. (a) Time evolution of the total hole density. (b) Time evolution of average projection probabilities. P^O: the outermost four KSOs. P^I: the remaining inner KSOs. (c) Time evolution of instantaneous energy expectation values for the propagating KSOs. Red curves: the outermost four KSOs (two-fold degenerate), forming the outermost energy shell (E^O). Blue curves: the remaining four inner KSOs forming the inner energy shell (E^I). Dashed lines are drawn to guide the eyes.

the other two π orbitals parallel to the yz plane do not show significant contributions. This is not a surprise because, as shown in Fig. 1, most parts of the CDFT holes are initialized in the π system parallel to the xz plane and only a bit are parallel to the yz plane. We also identify similar collective behaviors in more complicated $[BrC_4H]^+$ in Fig. 11 in Appendix C.

In a normal (TD)DFT, the electronic occupation number is either 1 or 0, manifesting whether the corresponding KSO is fully occupied. However, we find that the mode, as well as the mechanism of the electronic collective motion, can be identified in ensembles. The results in Fig. 6 are carried out using the ensemble-TDDFT with fractional occupation numbers [72–74]. For the $[BrC_2H]^+$, each spin channel of the HOMO is half occupied so that the symmetry between the two spin channels is preserved. As shown in Fig. 6(a), we identify a mode from the halogen site to the C-C bond, with a CM time of $\sim$0.66 fs, shorter than that by using integer occupations. In Fig. 6(b), we compute the average projection probabilities for the outermost four KSOs (P^O) and the rest of the inner KSOs (P^I). Similar to Fig. 5(b), the P^O evolves in concert with the hole migration, i.e., the peaks to the hole density on the Br site and the valleys to the hole density on the C-C
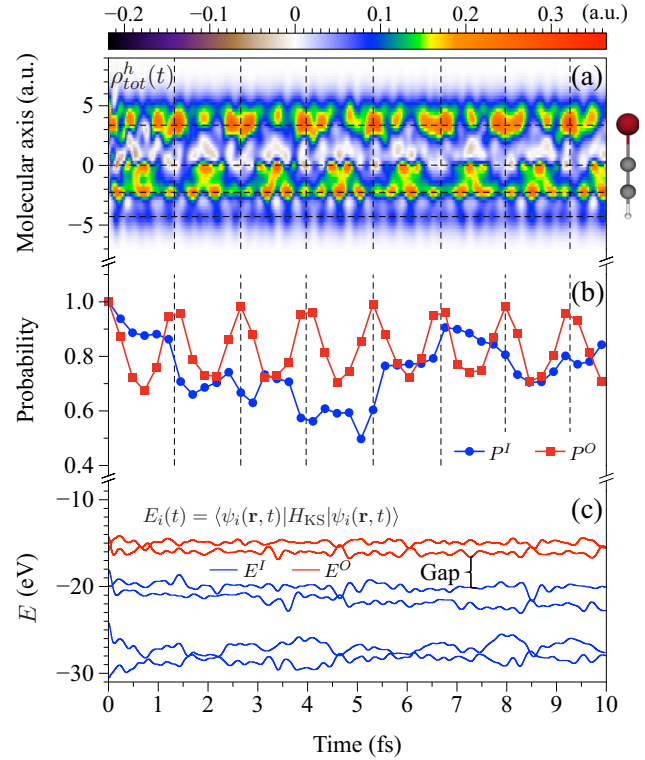
bond. In Fig. 6(c), it shows the time evolution of the instantaneous energy expectation values for the propagating KSOs. The outermost four KSOs (two-fold degenerate, forming the outermost energy shell E^O) depart from the rest of the inner KSOs (forming the inner energy shell E^I) with an energy gap of $\sim$3.5 eV, suggesting that the electron motion in the inner E^I shell may not be strongly coupling with that in the outermost E^O shell. To verify this, starting with the same CDFT initial state, we further calculate the CM dynamics by freezing the four lowest inner KSOs in the TD propagation. As shown in Fig. 7, an attosecond mode appears clearly with a CM time of $\sim$0.66 fs, in good agreement with the CM time produced by all eight KSOs. This again demonstrates that the electronic collective motion on the outermost orbital shell is responsible for the attosecond mode. More importantly, our frozen orbital calculations show that the mode can be solely driven by the nonlinear interaction of the outermost KSOs rather than by the interaction with the frozen inner KSOs.

IV. CONCLUSION

In summary, we studied the dynamical behavior of attosecond molecular modes in halogenated hydrocarbon chains based on the CDFT and TDDFT. It is found that the attosec-
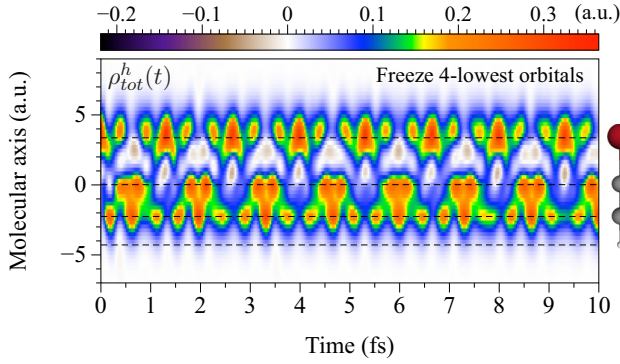
FIG. 7. The attosecond mode by freezing four lowest orbitals shown in Fig. 6. Dashed lines are drawn to guide the eyes.

ond mode is mainly recorded in the spin channel where the electron is initially ionized. Such a CM mode is sustainable, different from the fast spread of the hole density in hexatriene molecules [36]. To diagnose possible sources of error from approximate exchange-correlation functionals, we employed some widely used approximations, such as LDA, PBE, and PBE0. We found that the LDA works well to reproduce the attosecond mode, which does not show significant differences compared to more advanced functionals. By allowing the nuclei to relax, we found that the nuclear motion alters the mode via a fast smearing and detuning effect in a few femtoseconds. To get insight into the microscopic mechanism of the mode, we studied the electronic projection probabilities and instantaneous energy expectation values for propagated KS orbitals. We found that the mode is mainly attributed to the electronic collective motion in the outermost orbital shell, rather than any single-electron motion.

Since the outermost occupied molecular orbitals of large polyatomic molecules are usually conjugated π bonding, the findings in this work will be a heuristic for future experiments, such as the electric signal transduction in biomolecules or the molecular high-order harmonic generation.

APPENDIX A: DYNAMICAL PROPERTIES OF THE CM MODE IN [BrC$_4$H]$^+$ WITH LDA

As shown in Fig. 8(a), the attosecond CM mode in [BrC$_4$H]$^+$ involves a to-and-fro hole migration between the halogen and the terminal C-C bond, with a period of $\sim$2.08 fs. Figure 8(b) shows the average projection probability of the outermost six spin-up KSOs ($P_\uparrow^O$) and the rest of the six inner spin-up KSOs ($P_\uparrow^I$). Compared to the hole positions in Fig. 8(a), it is found that the peaks of the $P_\uparrow^O$ curves correspond to the hole localization on the Br site and the valleys of the $P_\uparrow^O$ curves correspond to the hole localization on the terminal C-C bond, suggesting the hole migration in the [BrC$_4$H]$^+$ is
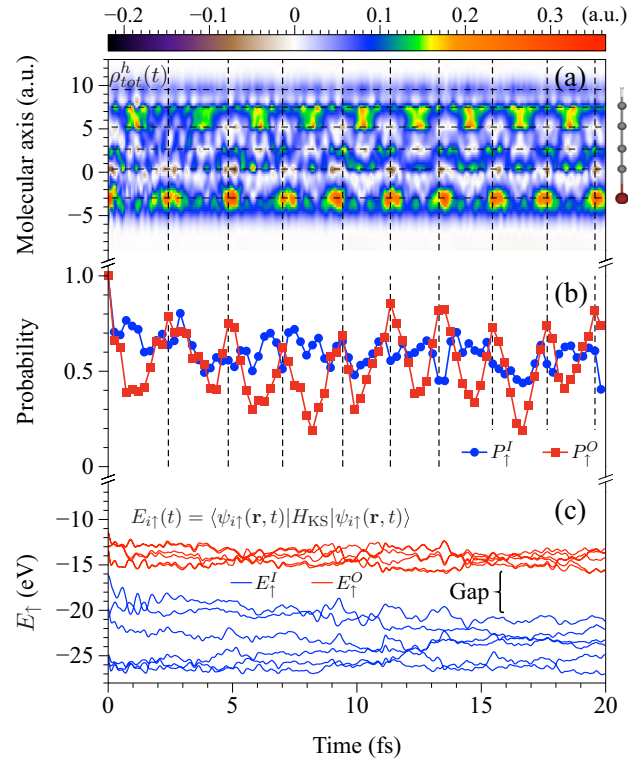

FIG. 8. Dynamical properties for the CM in the [BrC$_4$H]$^+$. (a) Time evolution of the total hole density. (b) Time evolution of average projection probabilities for the spin-up channel. $P_\uparrow^O$: the outermost six KSOs. $P_\uparrow^I$: the remaining six inner KS orbitals. (c) Time evolution of instantaneous energy expectation values for the propagated spin-up KSOs. Red curves: the outermost six KSOs. Blue curves: the remaining six inner KSOs.

attributed to the electronic collection motion on the outermost six spin-up KSOs. For the $P_\uparrow^I$ curves, we do not identify any clear concert with the hole migration. Figure 8(c) shows the instantaneous energy expectation values for propagated spin-up KSOs. The instantaneous energy expectation values for the outermost six KSOs lay on that for the rest of the six inner orbitals, divided with a wide energy gap of $\sim$5 eV, indicating the electronic motion in the outermost energy shell ($E_\uparrow^O$) may not be strongly affected by that in the inner energy shell ($E_\uparrow^I$).

APPENDIX B: KOHN-SHAM ORBITAL CONTRIBUTIONS TO THE SPIN-UP CM MODE IN [BrC$_2$H]$^+$ WITH LDA

Based on the hole definition in Eqs. (9) and (10), we define the KS orbital contribution along the molecular axis (i.e., the z axis)

$$\rho_{i,\sigma}^h(z,t) = \int \left[\rho_{i,\sigma}^0(x,y,z,t) - \rho_{i,\sigma}^+(x,y,z,t) \right] dx dy, \quad \text{(B1)}$$

where $\rho_{i,\sigma}^0$ is the neutral electronic density of the ith σ-spin KSO and $\rho_{i,\sigma}^+$ is the cationic electronic density of the ith σ-spin KSO. Therefore, $\rho_{i,\sigma}^h$ is the one-dimensional integrated hole density of the ith σ-spin KSO.
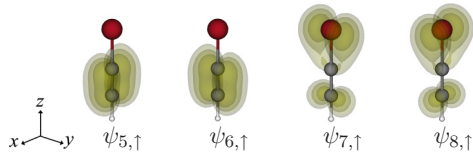
FIG. 9. Electronic density distributions of outermost four spin-up KSOs of the $[BrC_2H]^+$ initialized by the CDFT with LDA. Isovalues: 0.005, 0.01, 0.02 a_0^{-3}.

As shown in Fig. 9, for the spin-up channel, the outermost orbital shell of the $[BrC_2H]^+$ has four KSOs, labeled by $\psi_{5,\uparrow}$, $\psi_{6,\uparrow}$, $\psi_{7,\uparrow}$, and $\psi_{8,\uparrow}$. The orbital $\psi_{5,\uparrow}$ and $\psi_{8,\uparrow}$ distribute parallel to the xz plane and the $\psi_{6,\uparrow}$ and $\psi_{7,\uparrow}$ parallel to the yz plane. Note that $\psi_{8,\uparrow}$ is unoccupied due to its empty electronic populations, i.e., $f_{8,\uparrow} = 0$, while other orbitals are fully occupied, i.e., $f_{i,\sigma} = 1$.

As shown in Fig. 10, we classify the orbital hole density for into two categories. One is parallel to the xz plane, labeled by $\rho_{5,\uparrow}^h + \rho_{8,\uparrow}^h$ in Fig. 10(a). The other is parallel to the yz plane, labeled by $\rho_{6,\uparrow}^h + \rho_{7,\uparrow}^h$ in Fig. 10(b). Parallel to the xz plane, the $\rho_{5,\uparrow}^h + \rho_{8,\uparrow}^h$ forms a clear and uncluttered hole migration from the initial Br site to the terminal C-C bond and negative
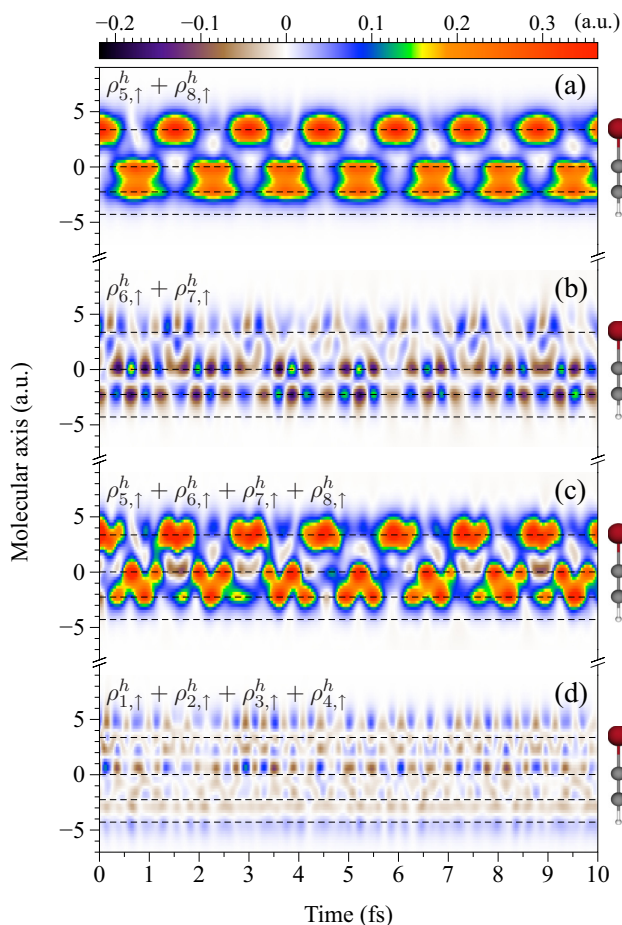
parts of the holes are difficult to be found. However, parallel the yz plane, the $\rho_{6,\uparrow}^h + \rho_{7,\uparrow}^h$ shows that most parts of positive and negative holes cancel each other. Comparing with the summation in Fig. 10(c), we can observe that the $\rho_{6,\uparrow}^h + \rho_{7,\uparrow}^h$ still have nonnegligible contributions, which act as an embellishment to the CM mode. As expected, Fig. 10(d) shows that the inner four KSOs do not have evident contributions to the CM mode.

APPENDIX C: KOHN-SHAM ORBITAL CONTRIBUTIONS TO THE SPIN-UP CM MODE IN $[BrC_4H]^+$ WITH LDA

According to Eq. (B1), we separate the spin-up CM mode of $[BrC_4H]^+$ into its orbital components. The outermost shell consists of 6 KSOs, labeled by $\psi_{7,\uparrow}$, $\psi_{8,\uparrow}$, $\psi_{9,\uparrow}$, $\psi_{10,\uparrow}$, $\psi_{11,\uparrow}$, and $\psi_{12,\uparrow}$. These KSOs can be classified into two categories. One is the $\psi_{7,\uparrow}$, $\psi_{9,\uparrow}$, and $\psi_{12,\uparrow}$ parallel to the xz plane. The other is the $\psi_{8,\uparrow}$, $\psi_{10,\uparrow}$, and $\psi_{11,\uparrow}$ parallel to the yz plane. Note that the $\psi_{12,\uparrow}$ is unoccupied due to its empty electronic occupation, while the other KSOs are fully occupied.

In Fig. 11(a), we find that the summation $\rho_{8,\uparrow}^h + \rho_{10,\uparrow}^h + \rho_{11,\uparrow}^h$ does not show any evident modes. On the
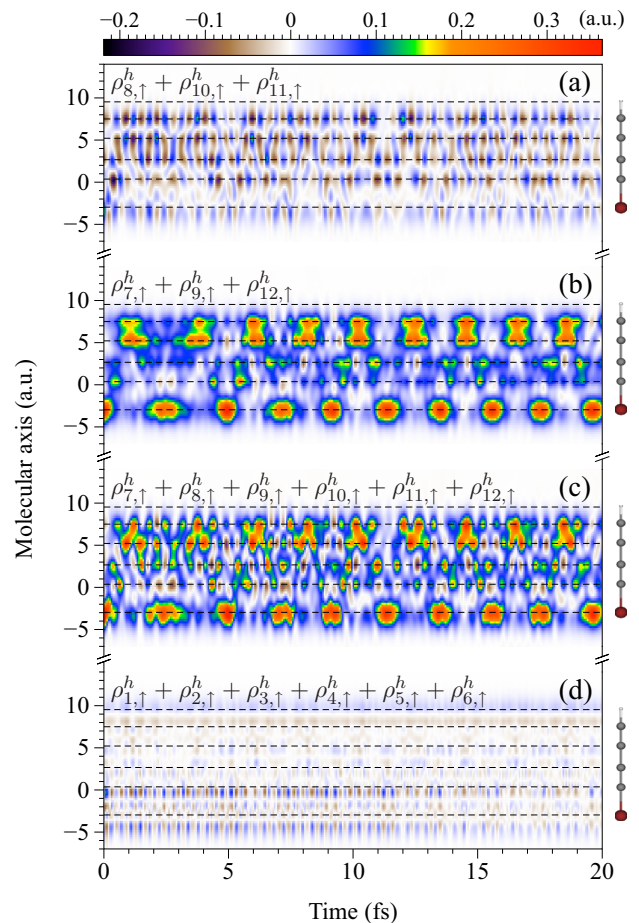

FIG. 10. Time evolution of orbital-resolved hole density of the $[BrC_2H]^+$ with LDA, for (a) $\rho_{5,\uparrow}^h + \rho_{8,\uparrow}^h$, (b) $\rho_{6,\uparrow}^h + \rho_{7,\uparrow}^h$, (c) the summation of orbital hole densities of outermost four KSOs and (d) the summation of orbital hole densities of inner four KSOs.

FIG. 11. Time evolution of orbital-resolved hole density of the $[BrC_4H]^+$ with LDA, for (a) $\rho_{8,\uparrow}^h + \rho_{10,\uparrow}^h + \rho_{11,\uparrow}^h$, (b) $\rho_{7,\uparrow}^h + \rho_{9,\uparrow}^h + \rho_{12,\uparrow}^h$, (c) the summation of orbital hole densities of outermost six KSOs, and (d) the summation of orbital hole densities of inner six KSOs.

contrary, in Fig. 11(b), $\rho^h_{7,\uparrow} + \rho^h_{9,\uparrow} + \rho^h_{12,\uparrow}$ contributes a clear hole mode from the Br to the terminal C-C bond, synchronous with the CM mode. Comparing with Fig. 11(c), we find the $\rho^h_{8,\uparrow} + \rho^h_{10,\uparrow} + \rho^h_{11,\uparrow}$ slightly mod-

ifies hole patterns in Fig. 11(b). In addition, Fig. 11(d) does not show evident patterns, demonstrating that the spin-up CM mode is mainly attributed to the outermost six KSOs.

[1] F. Krausz and M. Ivanov, Rev. Mod. Phys. **81**, 163 (2009).

[2] M. Nisoli, P. Decleva, F. Calegari, A. Palacios, and F. Martín, Chem. Rev. **117**, 10760 (2017).

[3] P. M. Kraus, M. Zürch, S. K. Cushing, D. M. Neumark, and S. R. Leone, Nat. Rev. Chem. **2**, 82 (2018).

[4] E. Goulielmakis, Z.-H. Loh, A. Wirth, R. Santra, N. Rohringer, V. S. Yakovlev, S. Zherebtsov, T. Pfeifer, A. M. Azzeer, M. F. Kling *et al.*, Nature (London) **466**, 739 (2010).

[5] M. F. Kling, P. von den Hoff, I. Znakovskaya, and R. de Vivie-Riedle, Phys. Chem. Chem. Phys. **15**, 9448 (2013).

[6] J. Yang, X. Zhu, J. P. F. Nunes, J. K. Yu, R. M. Parrish, T. J. Wolf, M. Centurion, M. Gühr, R. Li, Y. Liu *et al.*, Science **368**, 885 (2020).

[7] P. Peng, C. Marceau, and D. M. Villeneuve, Nat. Rev. Phys. **1**, 144 (2019).

[8] P. M. Kraus, B. Mignolet, D. Baykusheva, A. Rupenyan, L. Horný, E. F. Penka, G. Grassi, O. I. Tolstikhin, J. Schneider, F. Jensen *et al.*, Science **350**, 790 (2015).

[9] H. Yong, S. M. Cavaletto, and S. Mukamel, J. Phys. Chem. Lett. **12**, 9800 (2021).

[10] L. S. Cederbaum and J. Zobeley, Chem. Phys. Lett. **307**, 205 (1999).

[11] F. Calegari, D. Ayuso, A. Trabattoni, L. Belshaw, S. De Camillis, S. Anumula, F. Frassetto, L. Poletto, A. Palacios, P. Decleva *et al.*, Science **346**, 336 (2014).

[12] M. Lara-Astiaso, D. Ayuso, I. Tavernelli, P. Decleva, A. Palacios, and F. Martín, Faraday Discuss. **194**, 41 (2016).

[13] I. Polyak, A. J. Jenkins, M. Vacher, M. E. Bouduban, M. J. Bearpark, and M. A. Robb, Mol. Phys. **116**, 2474 (2018).

[14] E. P. Månsson, S. Latini, F. Covito, V. Wanie, M. Galli, E. Perfetto, G. Stefanucci, H. Hübener, U. De Giovannini, M. C. Castrovilli *et al.*, Commun. Chem. **4**, 73 (2021).

[15] V. Despré, N. V. Golubev, and A. I. Kuleff, Phys. Rev. Lett. **121**, 203002 (2018).

[16] F. Remacle and R. D. Levine, Proc. Natl. Acad. Sci. USA **103**, 6793 (2006).

[17] R. Weinkauf, P. Schanen, A. Metsala, E. Schlag, M. Bürgle, and H. Kessler, J. Phys. Chem. **100**, 18567 (1996).

[18] F. Lépine, M. Y. Ivanov, and M. J. Vrakking, Nat. Photonics **8**, 195 (2014).

[19] L. He, S. Sun, P. Lan, Y. He, B. Wang, P. Wang, X. Zhu, L. Li, W. Cao, P. Lu *et al.*, Nat. Commun. **13**, 4595 (2022).

[20] D. T. Matselyukh, V. Despré, N. V. Golubev, A. I. Kuleff, and H. J. Wörner, Nat. Phys. **18**, 1206 (2022).

[21] F. Remacle and R. Levine, J. Chem. Phys. **110**, 5089 (1999).

[22] S. Lünnemann, A. I. Kuleff, and L. S. Cederbaum, Chem. Phys. Lett. **450**, 232 (2008).

[23] A. I. Kuleff, S. Lünnemann, and L. S. Cederbaum, Chem. Phys. **414**, 100 (2013).

[24] M. Vacher, M. J. Bearpark, and M. A. Robb, J. Chem. Phys. **140**, 201102 (2014).

[25] F. Calegari, D. Ayuso, A. Trabattoni, L. Belshaw, S. De Camillis, F. Frassetto, L. Poletto, A. Palacios, P. Decleva, J. B. Greenwood *et al.*, IEEE J. Sel. Top. Quan. Electron. **21**, 8700512 (2015).

[26] M. Vacher, M. J. Bearpark, M. A. Robb, and J. P. Malhado, Phys. Rev. Lett. **118**, 083001 (2017).

[27] M. Lara-Astiaso, A. Palacios, P. Decleva, I. Tavernelli, and F. Martín, Chem. Phys. Lett. **683**, 357 (2017).

[28] A. Bruner, S. Hernandez, F. Mauger, P. M. Abanador, D. J. LaMaster, M. B. Gaarde, K. J. Schafer, and K. Lopata, J. Phys. Chem. Lett. **8**, 3991 (2017).

[29] N. V. Golubev, T. Begušić, and J. Vaníček, Phys. Rev. Lett. **125**, 083001 (2020).

[30] F. Khalili, M. Vafaee, D. Cho, and B. Shokri, Int. J. Quan. Chem. **121**, e26754 (2021).

[31] A. S. Folorunso, A. Bruner, F. Mauger, K. A. Hamer, S. Hernandez, R. R. Jones, L. F. DiMauro, M. B. Gaarde, K. J. Schafer, and K. Lopata, Phys. Rev. Lett. **126**, 133002 (2021).

[32] K. A. Hamer, F. Mauger, A. S. Folorunso, K. Lopata, R. R. Jones, L. F. DiMauro, K. J. Schafer, and M. B. Gaarde, Phys. Rev. A **106**, 013103 (2022).

[33] F. Mauger, A. S. Folorunso, K. A. Hamer, C. Chandre, M. B. Gaarde, K. Lopata, and K. J. Schafer, Phys. Rev. Res. **4**, 013073 (2022).

[34] M. Vacher, L. Steinberg, A. J. Jenkins, M. J. Bearpark, and M. A. Robb, Phys. Rev. A **92**, 040502(R) (2015).

[35] M. Lara-Astiaso, M. Galli, A. Trabattoni, A. Palacios, D. Ayuso, F. Frassetto, L. Poletto, S. De Camillis, J. Greenwood, P. Decleva *et al.*, J. Phys. Chem. Lett. **9**, 4570 (2018).

[36] A. D. Dutoi, M. Wormit, and L. S. Cederbaum, J. Chem. Phys. **134**, 024303 (2011).

[37] S. Fleischer, Y. Zhou, R. W. Field, and K. A. Nelson, Phys. Rev. Lett. **107**, 163603 (2011).

[38] B. Kaduk, T. Kowalczyk, and T. Van Voorhis, Chem. Rev. **112**, 321 (2012).

[39] Q. Wu and T. Van Voorhis, J. Chem. Theo. Comput. **2**, 765 (2006).

[40] B. Kaduk and T. Van Voorhis, J. Chem. Phys. **133**, 061102 (2010).

[41] G. Moynihan, G. Teobaldi, and D. D. O'Regan, Phys. Rev. B **94**, 220104(R) (2016).

[42] H. Eshuis and T. Van Voorhis, Phys. Chem. Chem. Phys. **11**, 10293 (2009).

[43] E. Runge and E. K. U. Gross, Phys. Rev. Lett. **52**, 997 (1984).

[44] H. Hu, N. Li, P. Liu, R. Li, and Z. Xu, Phys. Rev. Lett. **119**, 173201 (2017).

[45] A. Dreuw, J. L. Weisman, and M. Head-Gordon, J. Chem. Phys. **119**, 2943 (2003).

[46] C. M. Isborn and X. Li, J. Chem. Phys. **129**, 204107 (2008).

[47] M. Lein and S. Kümmel, Phys. Rev. Lett. **94**, 143003 (2005).

[48] E. Ruiz, S. Alvarez, J. Cano, and V. Polo, J. Chem. Phys. **123**, 164110 (2005).

[49] P. Mori-Sánchez, A. J. Cohen, and W. Yang, J. Chem. Phys. **125**, 201102 (2006).

[50] R. van Leeuwen and E. J. Baerends, Phys. Rev. A **49**, 2421 (1994).

[51] N. T. Maitra and K. Burke, Phys. Rev. A **63**, 042501 (2001).

[52] W. Kohn and L. J. Sham, Phys. Rev. **140**, A1133 (1965).

[53] Q. Wu and T. Van Voorhis, Phys. Rev. A **72**, 024502 (2005).

[54] D. D. O'Regan and G. Teobaldi, Phys. Rev. B **94**, 035159 (2016).

[55] D. Kidd, A. S. Umar, and K. Varga, Phys. Rev. B **98**, 075108 (2018).

[56] R. S. Mulliken, J. Chem. Phys. **23**, 1833 (1955).

[57] A. E. Clark and E. R. Davidson, Int. J. Quan. Chem. **93**, 384 (2003).

[58] A. D. Becke, J. Chem. Phys. **88**, 2547 (1988).

[59] F. L. Hirshfeld, Theor. Chim. Acta **44**, 129 (1977).

[60] N. Tancogne-Dejean, M. J. Oliveira, X. Andrade, H. Appel, C. H. Borca, G. Le Breton, F. Buchholz, A. Castro, S. Corni, A. A. Correa *et al.*, J. Chem. Phys. **152**, 124119 (2020).

[61] C. Hartwigsen, S. Goedecker, and J. Hutter, Phys. Rev. B **58**, 3641 (1998).

[62] J. P. Perdew and A. Zunger, Phys. Rev. B **23**, 5048 (1981).

[63] P. Ehrenfest, Z. Phys. **45**, 455 (1927).

[64] F. Calvayrac, P.-G. Reinhard, E. Suraud, and C. Ullrich, Phys. Rep. **337**, 493 (2000).

[65] A. Gomez Pueyo, M. A. Marques, A. Rubio, and A. Castro, J. Chem. Theory Comput. **14**, 3040 (2018).

[66] J. P. Perdew, K. Burke, and M. Ernzerhof, Phys. Rev. Lett. **77**, 3865 (1996).

[67] C. Adamo and V. Barone, J. Chem. Phys. **110**, 6158 (1999).

[68] M. Ernzerhof and G. E. Scuseria, J. Chem. Phys. **110**, 5029 (1999).

[69] A. J. Jenkins, M. Vacher, R. M. Twidale, M. J. Bearpark, and M. A. Robb, J. Chem. Phys. **145**, 164103 (2016).

[70] M. Vacher, F. E. Albertani, A. J. Jenkins, I. Polyak, M. J. Bearpark, and M. A. Robb, Faraday Discuss. **194**, 95 (2016).

[71] D. Jia, J. Manz, and Y. Yang, J Phys Chem. Lett. **10**, 4273 (2019).

[72] T. Li and Y. Li, Phys. Rev. A **31**, 3970 (1985).

[73] J.-D. Chai, J. Chem. Phys. **136**, 154104 (2012).

[74] T. Gould, G. Stefanucci, and S. Pittalis, Phys. Rev. Lett. **125**, 233001 (2020).